48th AIAA Aerospace Sciences Meeting Including the New Horizons Forum and Aerospace Exposition
4 - 7 January 2010, Orlando, Florida

AIAA 2010-227

Numerical Study of Magnetoaerodynamic Flow around a Hemisphere

Nicholas J. Bisek* and Iain D. Boyd†

Department of Aerospace Engineering, University of Michigan, Ann Arbor, MI, 48109, USA

and

Jonathan Poggie‡

Air Force Research Laboratory, Wright-Patterson AFB, OH, 45433-7512, USA

Newly developed computational tools are used to compute hypersonic flow around a hemisphere capped geometry which utilizes a magnet located within the body as a means of heat flux mitigation. These tools include an improved electrical conductivity model and a parallelized 3D magnetohydrodynamic module that is loosely coupled to a 3D fluid code. Results show the shock standoff distance increases when the magnetic field is applied. The change in shock standoff distance is consistent with experimental measurements. The increase in shock standoff distance reduces the gradients in the shock layer thereby reducing the peak heat flux to the body. However, the total heat flux increases due to increased heating on the aft section of the geometry.

Nomenclature

ρ = mass density
μ = coefficient of viscosity
u = streamwise velocity component
$\mathbf{u}$ = velocity vector (u, v, w)
x, y, z = streamwise, spanwise, and transverse coordinates
N = total number density, m^{-3}
p = pressure
$\mathbf{I}$ = identity matrix
τ = viscous stress
δ_{ij} = delta operator, $\delta_{ij} = \begin{cases} 1, i=j \\ 0, i \neq j \end{cases}$
E = total energy per volume
$\mathbf{q}$ = heat flux (translational, rotational, and vibrational)
T = temperature
L = geometry length
Re_m = magnetic Reynolds number, uL/η_m
η_m = magnetic diffusivity, $\mu_0^{-1}\sigma^{-1}$
μ_0 = permeability of free space, $4\,\pi \times 10^{-7}$ $\mathrm{N/A^2}$
ν_m = electron-neutral particle collision frequency
m_e = electron mass, 9.11×10^{-31}kg
e = electron charge, 1.6×10^{-19}C
σ = electrical conductivity, $\Omega^{-1}\mathrm{m}^{-1}$
$\tilde{\sigma}$ = electrical conductivity tensor (including Hall effect)
α = degree of ionization

*Graduate Student, Student Member AIAA.
†Professor, Associate Fellow AIAA.
‡Senior Aerospace Engineer, AFRL/RBAC. Associate Fellow AIAA.

Q = collision cross-section, cm^2
ϕ = electric potential, V
$\mathbf{B}$ = magnetic field vector
B = magnetic field magnitude, T
$\mathbf{E}$ = electric field vector
E = electric field magnitude, $\mathrm{V/m}$
$\mathbf{j}$ = current density vector
r = radius
β = Hall parameter, $\sigma \mathrm{B}/[en_\mathrm{e}]$
n = species number density, m^{-3}
χ = species mole fraction
$\mathrm{C_p}$ = pressure coefficient, $[2(p_w - p_\infty)]/[\rho_\infty u_\infty^2]$
$\mathrm{C_h}$ = nondimensional heat flux, $2q_w/[\rho_\infty u_\infty^3]$

Subscript
∞ = free stream
w = wall
n = nose

Species
Ar = argon
Ar^+ = argon ion
e = electron

I. Introduction

The idea of using an applied magnetic field to reduce the heat transfer to a hypersonic vehicle has been a topic of scientific research since the late 1950's when Kantrowitz[1] and Resler and Sears[2,3] conducted the first calculations demonstrating the potential benefits an applied magnetic field has on an incoming weakly ionized flow, a condition typically observed during re-entry. The magnetic field, if properly aligned, creates a magnetic force which opposes the incoming flow, effectively increasing the shock standoff distance. The thickening of the shock layer reduces the gradients near the stagnation point, and thus lowers the peak heat transfer rate.

In the midst of the space race, this novel idea attracted a lot of attention as many groups looked to further explore and refine the semi-analytical calculations by making various approximations to the conservation equations. Of these efforts, the work by Bush[4,5] is considered to be one of the most complete approximate analytic solutions.[6] Bush's approach used a local solution at the stagnation point of the hypersonic flow over an axisymmetric blunt body, and predicted significant flow deceleration with the presence of a magnetic field. The first modern computational fluid dynamic (CFD) simulations of the magnetohydrodynamic (MHD) blunt body problem were completed about a decade later by Coakley and Porter.[7] Because of the lack of computational resources at the time, the simulations still required significant simplifications, including that the gas was ideal, non-reacting, and inviscid.

The first experimental work to complement the computational activity was completed by Ziemer[8] and focused on measuring the shock standoff distance. Bush's approximate results were in reasonable agreement with these first experiments. The first heat transfer measurements for this concept were collected in the experimental work by Wilkinson[9] for Mach 3 ionized argon at the stagnation point of a blunt cone.

Another experimental effort was conducted by Kranc *et al.*[10] in the late 1960's. This work provided additional experimental validation sets for the continuing computational efforts, as it explored shock standoff distance and drag measurements for hypersonic flow over two different axisymmetric geometries. These experiments were run in a flow regime where both the viscosity and Hall effect are important, and confirmed the increase in the shock standoff distance and total drag on the geometry in the presence of a dipole magnetic field. The experiments also exhibited an increase in total heating, which has been attributed to the Hall effect.[11,12] This was unexpected because the thickening of the shock layer reduces gradients within the stagnation region, which should reduce the heat flux to the body. Previous semi-analytic work had predicted that the Hall effect would only reduce the effectiveness of the magnetic force on increasing the shock standoff

distance and total drag.[13] Regardless of this unexpected outcome, it was determined that the large magnetic field strength needed to make the technology practical required a magnet that was too heavy to be placed on re-entry vehicles and the research area faded.[14]

While hypersonic research continued to experience strong support through the rest of the twentieth century due, in part, to various programs like Apollo and Shuttle,[15]a it was not until the mid-1990's that interest in plasma-assisted hypersonic flow control started to reappear.[16–18] This resurgence has been credited to many factors including the increasing demand for sustained hypersonic flight, rapid access to space, and numerous mechanical and material advances in the area of flight-weight MHD technologies. One of the first to reevaluate the technology using modern CFD was Palmer,[19] who performed first-order spatially accurate simulations of the time-dependent Maxwell's equations coupled to the Navier-Stokes equations to analyze a Mars return vehicle.

The rising costs for hypersonic experiments and the need for results within a greater range of flow-field conditions for increasing geometric complexity has continued to motivate the development of computational tools that are capable of accurately computing these plasma-based hypersonic flow control devices. This need has spurred numerous computational studies in the recent years exploring all aspects of plasma-based flow enhancements including flow control,[20–25] local heat load mitigation,[26–28] communications blackout,[29,30] and MHD power extraction.[31–33]

Despite the large financial costs, limited facilities, and technical challenges, some recent experimental studies have been performed by Lineberry *et al.*,[34] Takizawa *et al.*,[35] Kimmel *et al.*,[36] Matsuda *et al.*,[37] and Gülhan *et al.*[38] to explore electromagnetic effects on hypersonic flows. While these efforts have provided new insight into electromagnetic phenomena in hypersonic flows, more precise measurements, and additional validation exercises for testing the accuracy of fluid-MHD codes, the rising costs (increased maintenance for aging facilities and additional safety protocol), associated with conducting hypersonic experiments greatly limits the number of experiments being conducted.

At the same time, supercomputing systems continue to experience exponential performance increases with substantial decreases in cost. This has led to a continued increase in computational research. In fact, Padilla estimates that if current trends continue, over 70% of hypersonic research will involve computational analysis by 2020.[15]

This work focuses on the previously mentioned experiment conducted by Kranc *et al.*[10] and Bush's semi-analytical effort.[4,5] Bush's computational work was previously explored computationally by Poggie and Gaitonde[39–41] and Damevin and Hoffmann.[42] In the work by Poggie and Gaitonde, several of Bush's simplifications were removed and the Hall effect was added and investigated, while Damevin and Hoffmann explored chemistry effects for a single temperature model. In both efforts, a simplified model was used to estimate the flow's electrical conductivity. The present work extends these efforts by investigating several electrical conductivity models, including a surrogate model of solutions to Boltzmann's equation. The results show the percent change in shock standoff distance, due to the presence of the magnetic field, corresponds very well with the experimental measurements, especially when employing the surrogate electrical conductivity model. In addition, the solutions show an increase in total heating to the geometry, which is consistent with the observations made by Nowak *et al.*[11,12] The increase in total heating is due to a slight increase in heating on the cylinder (aft) section of the geometry.

II. Method

A. Governing Equations

Flow-field results are obtained using Computational Fluid Dynamics (CFD) to solve the Navier-Stokes equations. The CFD computations are executed using the Michigan Aerothermodynamic Navier-Stokes (LeMANS) code which was developed at the University of Michigan.[43,44]

LeMANS is a general 2D/axisymmetric/3D, parallel, unstructured finite-volume CFD code. The numerical fluxes between cells are discretized using a modified Steger-Warming Flux Vector Splitting (FVS) scheme, except near shock waves. In these regions the original Steger-Warming FVS scheme is used because it provides sufficient dissipation to accommodate the discontinuity.[45] LeMANS is able to employ a two-temperature or three-temperature model to account for thermal-nonequilibrium and a standard finite rate chemistry model for non-equilibrium chemistry. The two-temperature model assumes a single temperature, T, accounts for the translational and rotational energy modes of all species, while the vibrational energy mode is accounted for by a separate temperature, T_{ve}. In the three-temperature model, the rotational energy

mode is independent of the translational energy mode.[46]

For a single temperature (local thermal equilibrium) model with MHD, but without finite chemistry, the conservation equations are:

$$\frac{\partial \rho}{\partial t} + \nabla \cdot (\rho \mathbf{u}) = 0 \tag{1}$$

$$\frac{\partial \rho \mathbf{u}}{\partial t} + \nabla \cdot (\rho \mathbf{u}\mathbf{u} + p\mathbf{I} - \tau) = \mathbf{j} \times \mathbf{B} \tag{2}$$

$$\frac{\partial E}{\partial t} + \nabla \cdot ((E + p)\mathbf{u} - \tau \cdot \mathbf{u} - \mathbf{q}) = \mathbf{j} \cdot \mathbf{E} \tag{3}$$

where $\mathbf{uu}$ in the conservation of momentum equation (2), is the 3×3 tensor containing all the products of the components of the velocity vector as seen in equation (4).

$$\mathbf{uu} = \begin{bmatrix} u^2 & uv & uw \\ vu & v^2 & vw \\ wu & wy & w^2 \end{bmatrix} \tag{4}$$

LeMANS assumes the fluid is continuous and Newtonian. It also assumes Stokes' hypothesis when determining the viscous stresses:

$$\tau_{ij} = \mu \left(\frac{\partial u_j}{\partial x_i} + \frac{\partial u_i}{\partial x_j} \right) - \frac{2}{3} \mu \nabla \cdot \mathbf{u} \delta_{ij}$$

The total energy deposition term, $\mathbf{j} \cdot \mathbf{E}$, appears on the right side of the total energy equation (3). The conservation of momentum equation is modified to include a magnetic force, $\mathbf{j} \times \mathbf{B}$, on the right hand side of equation (2). These additions constitute the effects the current density, $\mathbf{j}$, electric field, $\mathbf{E}$, and magnetic field, $\mathbf{B}$, have on the flow.

B. Low Magnetic Reynolds Number Approximation

The three additional variables appearing in the modified governing equations ($\mathbf{j}, \mathbf{B}$, and $\mathbf{E}$), are determined by first noting that the magnetic Reynolds number, equation (5), is small for the cases of interest.

$$Re_m = \frac{uL}{\eta_m} \tag{5}$$

Consequently, it can be shown that the induced magnetic field can be neglected.[47] This means only external magnetic fields are present in the flow (and must be specified). The current and electric fields are determined by solving the current continuity equation, which has the form of a Poisson equation as seen in equation (6).

$$\nabla \cdot \tilde{\sigma} \cdot [-\nabla \phi + \mathbf{u} \times \mathbf{B}] = 0 \tag{6}$$

where $\tilde{\sigma}$ is the electrical conductivity tensor, a compact way of accounting for the Hall effect[48] and is described in the next section. The electric potential, ϕ, is computed using a finite-volume method and appropriate boundary conditions as outlined in previous work.[49] The electric field is computed directly from the electric potential ($\mathbf{E} = -\nabla \phi$), which allows the electric current, $\mathbf{j}$, to be computed using a generalized form of Ohm's law ($\mathbf{j} = \tilde{\sigma} \cdot [\mathbf{E} + \mathbf{u} \times \mathbf{B}]$). Full details and validation of the magnetohydrodynamic solver are available in Ref. 49, while Ref. 50 provides details on its parallelization.

C. Hall Effect

As seen in equation (6), the MHD module incorporates the tensor nature of the electrical conductivity by following the computational work of Gaitonde and Poggie.[40,48] This approach provides a compact way of accounting for ion-slip and the Hall effect. While ion-slip is still assumed negligible for the scope of this paper, the Hall effect is not. Equation (7) shows the electrical conductivity tensor with the Hall effect for Cartesian coordinates:

$$\tilde{\sigma} = \frac{\sigma}{\mathrm{B}^2\,(1+\beta^2)} \begin{bmatrix} \mathrm{B}^2+\beta^2\,\mathrm{B}_x^2 & \beta\,(\beta\,\mathrm{B}_x\,\mathrm{B}_y - \mathrm{B}\,\mathrm{B}_z) & \beta\,(\beta\,\mathrm{B}_x\,\mathrm{B}_z + \mathrm{B}\,\mathrm{B}_y) \\ \beta\,(\beta\,\mathrm{B}_y\,\mathrm{B}_x + \mathrm{B}\,\mathrm{B}_z) & \mathrm{B}^2+\beta^2\,\mathrm{B}_y^2 & \beta\,(\beta\,\mathrm{B}_y\,\mathrm{B}_z - \mathrm{B}\,\mathrm{B}_x) \\ \beta\,(\beta\,\mathrm{B}_z\,\mathrm{B}_x - \mathrm{B}\,\mathrm{B}_y) & \beta\,(\beta\,\mathrm{B}_z\,\mathrm{B}_y + \mathrm{B}\,\mathrm{B}_x) & \mathrm{B}^2+\beta^2\,\mathrm{B}_z^2 \end{bmatrix} \tag{7}$$

where σ is the electrical conductivity of the fluid. B_x, B_y, and B_z are the components of the magnetic field vector and B is its magnitude. The Hall parameter, β, is defined in equation (8):

$$\beta = \frac{e\,\mathrm{B}}{m_\mathrm{e}\,\nu_m} \tag{8}$$

where an elemental charge $e = 1.6022 \times 10^{-19}$ C, the mass of an electron $m_\mathrm{e} = 9.11 \times 10^{-31}$ kg, and ν_m is the electron-neutral particle momentum transfer collision frequency which is related to the electrical conductivity in equation (9):

$$\nu_m = \frac{e^2\,n_\mathrm{e}}{m_\mathrm{e}\,\sigma} \tag{9}$$

where n_e is the electron number density. Equation (9) is combined with equation (8) to yield equation (10), which is directly computed from the fluid properties:

$$\beta = \frac{\sigma\,\mathrm{B}}{e\,n_\mathrm{e}} \tag{10}$$

Validation of the Hall effect is carried out by utilizing a computational study performed by Oliver and Mitchner.[51] In the experiment, finite segmented electrodes are infinitely repeated along the two walls of a channel as seen in Fig. 1. An externally applied magnetic field is positioned perpendicular to the channel velocity, **u**.

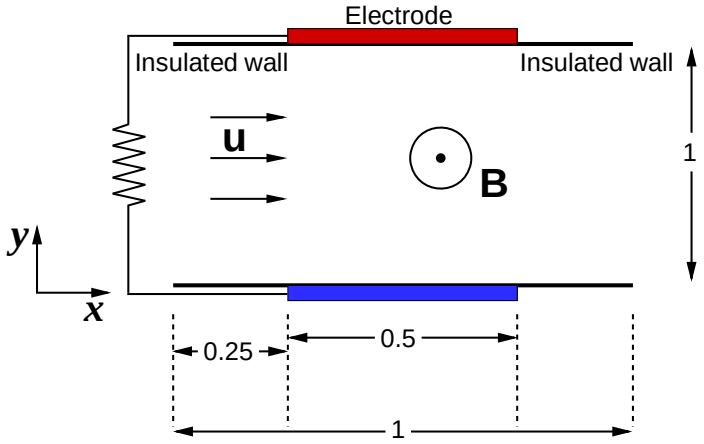

Figure 1. Schematic of the channel flow with finitely segmented electrodes. Units are in meters.

This exercise is inherently two-dimensional, but it is transformed into three dimensions by allowing the channel walls to be infinitely tall. Although this makes the problem computationally more expensive, the MHD routine is only suited for three-dimensional simulations. By using symmetric boundary conditions along the top and bottom planes of the domain, the actual height of the channel domain is set to a finite value of 0.1 m for the simulation, as seen in Fig. 2.

Because the channel is infinitely long, periodic boundary conditions are developed and employed at the domain inlet and outlet. The five point overlapping stencil, shown in Fig. 3, transfers information between the periodic inlet and outlet planes. The scheme is selected because it is well suited for structured grids and is straight-forward to implement when the entire domain is situated on a single processor (serial). In this approach, a row of cells starts at the inlet and ends at the outlet. Along this row, the periodic boundary conditions state that the values in the first two cells nearest the inlet (the ghost cell and adjoining real cell),

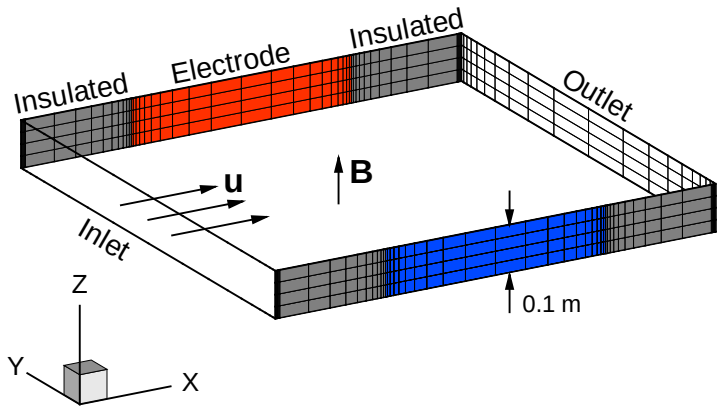

Figure 2. Geometry and boundary conditions for the 3D channel flow with finitely segmented electrodes. ($50 \times 20 \times 4$)

are set equal to the fifth and fourth cells from the outlet. These cells (the fifth and fourth cells from the outlet), along with the rest of the domain's interior cells, are determined by solving equation (6) numerically. Likewise, the last two cells in the row (the last real cell and its adjoining ghost cell), are set equal to the values in the fourth and fifth cells from the inlet.

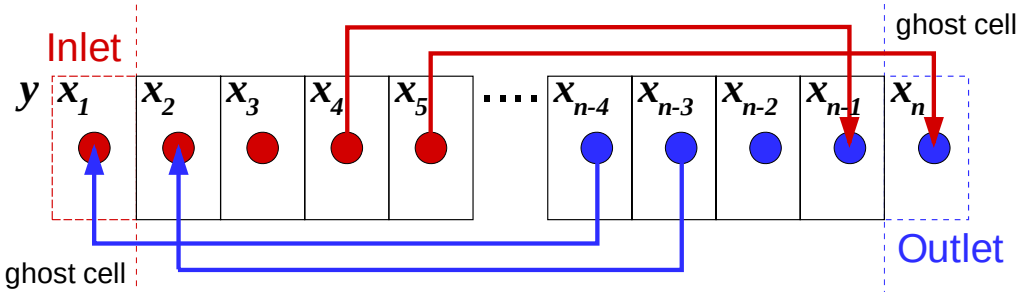

Figure 3. Cartoon of a five point stencil used for period boundary conditions.

Oliver and Mitchner carefully formulated this exercise so that the fluid velocity field did not affect the solution as long as $\nabla \times (\mathbf{u} \times \mathbf{B}) = 0$. For one iteration of the flow solver, the MHD routine is executed assuming the velocity profile is only a function of the distance between the plates $\mathbf{u} = f(y)$ which satisfies $\nabla \times (\mathbf{u} \times \mathbf{B}) = 0$ as long as $\mathbf{B} = f(z)$. The velocity profile is assumed to be fully developed Poiseuille flow between parallel plates,[52] as seen in equation (11):

$$\mathbf{u} = f(y) = u_{\max}(1 - \frac{(y - y_h)^2}{h^2}) \tag{11}$$

where $u_{\max}$ is the maximum velocity and is set to unity for this scenario ($u_{\max} = 1$ m/s). The y location is measured from the center of the channel width ($y_h = 0.5$ m) and $h = 0.5$ m is the channel half-width.

A grid independence study is performed using non-reacting argon with a constant electrical conductivity of $\sigma = 1\ \Omega^{-1}\text{m}^{-1}$. The channel walls are 1 m apart and the segmented electrodes are 0.5 m wide, with 0.5 m of insulated wall between them, so that the domain simulated has a length of 1 m in both the x and y-directions. The channel walls are set to a height of 0.1 m in the z-direction with symmetric boundaries applied at the $z = 0$, 0.1 m planes, effectively making the walls infinitely tall. Periodic boundaries are applied at the inlet and outlet, $x = 0$, 1 m, respectively.

The grid utilizes exponential spacing along the wall surface such that cell clustering occurs near the junction between the insulated wall and the electrode. Additionally, five uniform points are located near both the inlet and outlet (along the wall surfaces) to maintain smooth periodic boundary conditions. Exponential

spacing is also employed between the two walls such that cell clustering occurs near each surface. Uniform spacing is employed along the height of the wall (z-direction), as seen in Fig. 2. The 'coarse' grid employs 50 points along the wall ($x-$direction), 20 points between the walls ($y-$direction), and 4 points in the $z-$direction. Two additional, doubly refined grids are also developed: $100 \times 40 \times 8$ (medium), $200 \times 80 \times 16$ (fine).

Grid independence is assessed by comparing solutions of the electric potential, ϕ, for the scenario without a magnetic field ($\mathbf{B} = 0$). Since the wall is infinitely tall, the solution in the z-direction is constant and is only plotted along the $z = 0$ m plane. Extracting solutions of ϕ at two slices of the domain ($x = 0.25$, 0.5 m), Figs. 4(a) and 4(b) show the potential does not vary significantly between the 'medium' and 'fine' grids, so the 'medium' solution is considered grid-independent and is employed in the rest of the section.

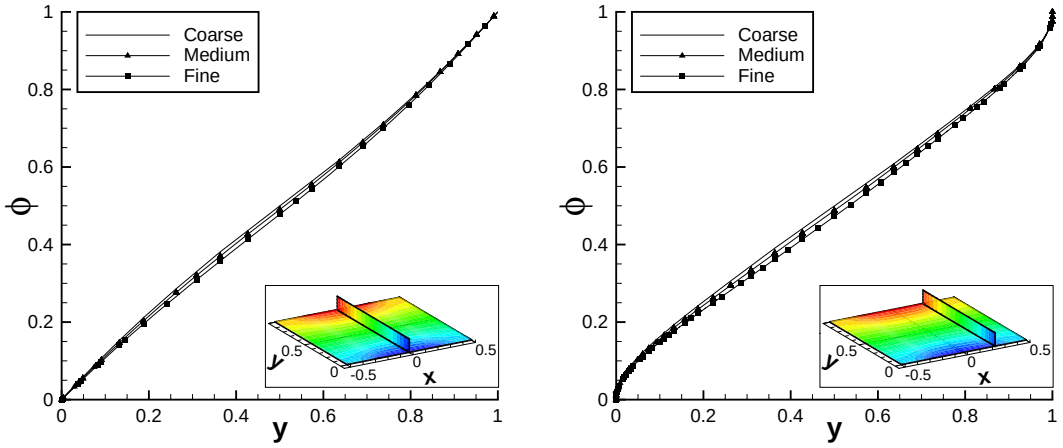

(a) $x = 0$ m (b) $x = 0.25$ m

Figure 4. Electric potential (ϕ), between two segmented electrodes at two different locations ($x = 0$ m and 0.25 m), for various grids. ($z = 0$ m)

Without the presence of the magnetic field, the Hall effect has no significance so the electrical conductivity tensor reverts to a scalar. The resultant electric potential solution is symmetric about the center of the electrode as seen in Fig. 5, where Fig. 5(a) is obtained by Gaitonde[40] and Fig. 5(b) is obtained using the 'medium' grid. Close examination of Figs. 5(a) and 5(b) shows that the results obtained are consistent, further validating the MHD solver.

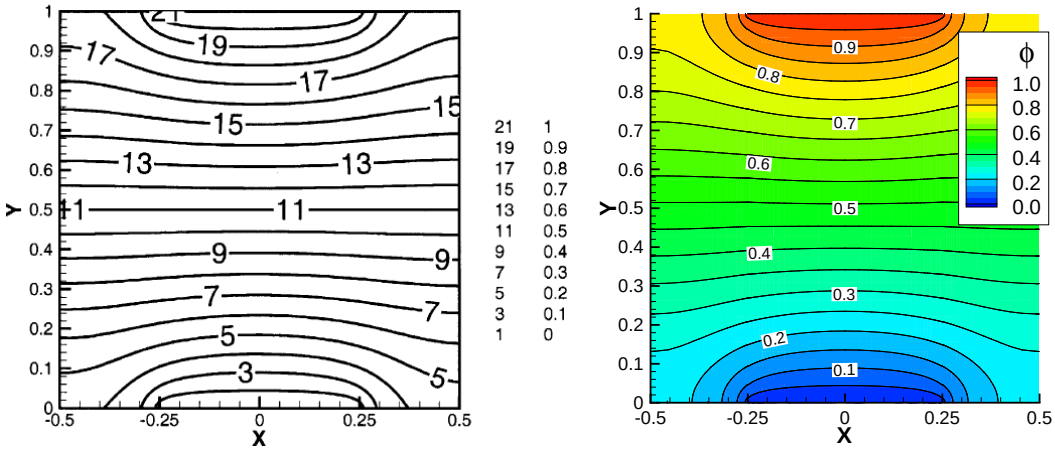

(a) From Gaitonde.[40] (b) Medium grid ($100 \times 40 \times 8$) at $z = 0$.

Figure 5. Electric potential contours for the segmented electrode channel without a magnetic field and constant electrical conductivity. ($\mathbf{B} = 0$, $\sigma = 1\ \Omega^{-1}\mathbf{m}^{-1}$)

To test the Hall effect, a second scenario is simulated. In this case, a nonzero magnetic field is externally applied. Consistent with the original analysis, the magnetic field is aligned with the z axis, whereas the velocity is aligned with the x axis. Without the Hall effect, a substantial current would only be created in the y direction. With the Hall effect, magnetic effects also appear in the off-diagonal components of the electrical conductivity tensor seen in equation (7). This results in the 'stretching' of the streamwise component of the current density vector, j_x, which becomes apparent by comparing the current density lines of Figs. 6(a) and 6(b). The results are also compared to the computational work by Gaitonde[40] in Fig. 6(c).

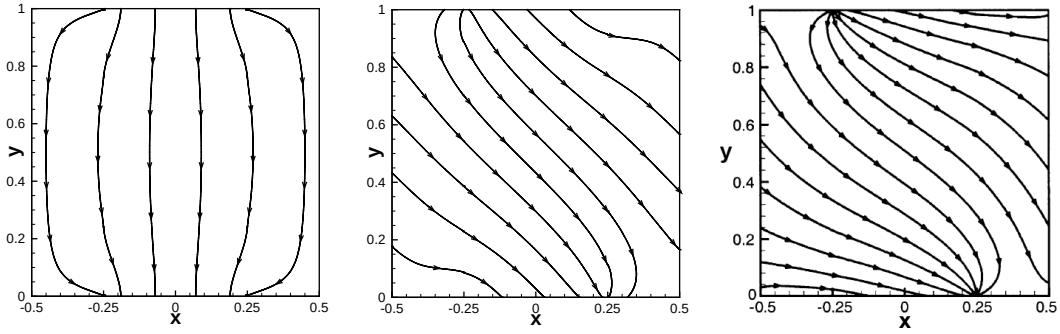

(a) Without the Hall effect (b) With the Hall effect (c) From Gaitonde.[40]

Figure 6. Current density streamlines j between two segmented electrodes with a magnetic field ($\mathbf{B}_z = 1$ T), constant electrical conductivity ($\sigma = 1\ \Omega^{-1}\mathbf{m}^{-1}$), and a streamwise velocity ($\mathbf{u} = f(y)$). ($100 \times 40 \times 8$)

The results obtained by Gaitonde in Fig. 6(c) do not exactly match the results shown in Fig. 6(b) because Gaitonde employed a nondimensional MHD formulation, which results in additional coefficients in his electrical conductivity vector. Nonetheless, both figures portray similar characteristics, and indicate that the Hall effect is successfully implemented.

D. Electrical Conductivity

The experiment performed by Kranc *et al.* used pre-ionized argon (Ar, Ar^+, and e). The electrical conductivity profile for weakly-ionized argon is shown in Fig. 7. As seen in the figure, the electrical conductivity exhibits two distinct regions, namely, weakly ionized ($T \lesssim 10{,}000$ K) and fully ionized ($T > 10{,}000$ K). Both regions display exponential growth versus temperature, which means a highly accurate conductivity model is important in order to accurately capture its behavior across the entire temperature range.

Three different electrical conductivity models are explored for this work. Raizer developed an electrical conductivity model that is an exponential function of temperature, assuming that electron-neutral collisions affect the conductivity more than the electron-ion collisions and that the ionization is in thermal equilibrium,[54] as seen in Eqn. 12:

$$\sigma = 83 \times e^{-36000/\mathrm{T}}\ \ \Omega^{-1}\mathrm{cm}^{-1} \tag{12}$$

where the temperature T is specified in Kelvin. This model is considered valid for air, nitrogen, and argon at p = 1 atm for a temperature range of 8000 to 14000 K. However, the model's coefficients (83 and -36000), can be adjusted depending on the temperature range, pressure, or gas composition of interest, but are used as specified for this study.

Chapman and Cowling[55] developed a model for a weakly-ionized gas by assuming there is a coupling between the charge and mass diffusion terms and that the resultant electron energy distribution function from solutions to Boltzmann's equation is only a function of this coupled, binary diffusion coefficient. This assumption results in a semi-analytic model for the electrical conductivity, as seen in Eqn. 13:

$$\sigma = 3.34 \times 10^{-12} \frac{\alpha}{Q\sqrt{\mathrm{T}}}\ \ \Omega^{-1}\mathrm{cm}^{-1} \tag{13}$$

where Q [cm^2] is the collision cross-section of the gas, and the degree of ionization $\alpha = {}^{\Sigma\, n_{\mathrm{ions}}}/_{N}$. One limitation of using the Chapman and Cowling model is that Q must be determined by an outside source (i.e., experimental data, reference tables, an ideal molecule approximation, etc.). For this work, the collision

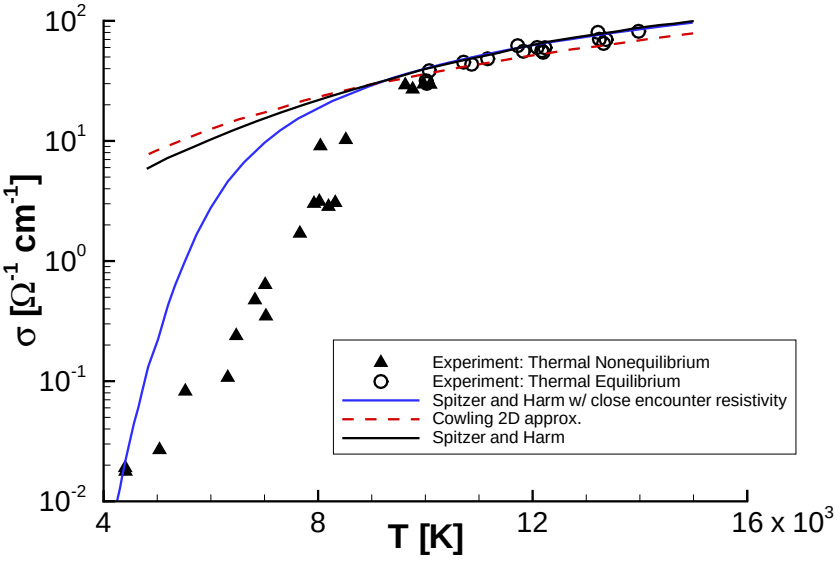

Figure 7. Electrical conductivity of argon ($p = 0.013$ atm), reproduced from Lin *et al.*[53]

cross-section is taken to be the total collision cross-section for argon-argon collisions using hard sphere model,[56] with a diameter of 4.04×10^{-10} m,[57] to yield: $Q \simeq 5 \times 10^{-17}$ cm^2. This assumption is made because it is unclear what the best choice for Q should be, and because this assumption produces results that are consistent with the other models in previous work.[49,50]

A surrogate model of solutions to Boltzmann's equation is the third electrical conductivity model studied. A 2$^{\text{nd}}$ order polynomial response surface is employed to capture the behavior of the solutions to Boltzmann's equations by developing a three-dimensional Design of Experiment (DOE). The solutions to Boltzmann's equation are determined using a Boltzmann solver developed by Kushner *et al.*,[58] which is functionally equivalent to that proposed by Rockwood.[59,60] The Boltzmann solver's input parameters, namely, E/N, χ_{Ar}, and χ_{Ar^+}, define the three-dimensions of the DOE (χ_{e} is unnecessary because of the assumed local charge neutrality). Details of this approach were discussed in previous work,[50] but have been modified to improve the accuracy of the model as described below.

With the DOE determined, solutions to the model's 'learning' and 'testing' points are obtained from individual Boltzmann solutions, while accounting for electron-electron collisions. Figure 8 plots the resulting electrical conductivity contours, which show a region of high conductivity for low χ_{Ar} (high degree of ionization), and a weak normalized electric field, E/N.

Decreasing electrical conductivity for an increasing electric field strength was also observed in previous work for the electrical conductivity of air.[49] As such, the electrical conductivity appears to be a function of E/N, which is anticipated by factoring the electron number density out of the definition of electrical conductivity for a DC current ($\sigma = {e^2}\, {n_{\text{e}}}/{m_{\text{e}}\, \nu_m}$), to yield: ${\sigma}/{n_{\text{e}}} \sim \nu_m^{-1}$. Since the electron collision frequency, ν_m, usually increases with increasing E/N, as seen in Fig. 9, the electrical conductivity should decrease with increasing electric field strength.

Since the model's dependent variable, σ, has a large range of values, the Polynomial Response Surface (PRS) surrogate model may have trouble capturing the behavior, especially in regions with a large gradient. An open-source MATLAB® library, *SURROGATES Toolbox*,[61] is used to create the PRS model. In order to improve the accuracy of the model, it is useful to transform the function that the PRS model is trying to mimic, by reducing the range of the dependent variable. Dividing the electrical conductivity by the degree of ionization does not require any additional information (parameters), since $\alpha = \Sigma\, \chi_{\text{ions}} = \chi_{\text{Ar}^+}$, but helps to normalize the solution. However, this leads to a division by zero error when $\alpha = 0$, so the dependent variable is inverted: ${\alpha}/{\sigma}$. This transformation is similar to the Chapman-Cowling model, which also utilizes the degree of ionization in the numerator. Unfortunately, this formulation has a small solution range for this scenario ($10^{-8}\ \Omega \cdot \text{m} \leq \alpha/\sigma \leq 10^{-6}\ \Omega \cdot \text{m}$), so the natural logarithm is also applied to renormalize the solution range. Equation (14) lists the model formulation provided to *SURROGATES Toolbox*:

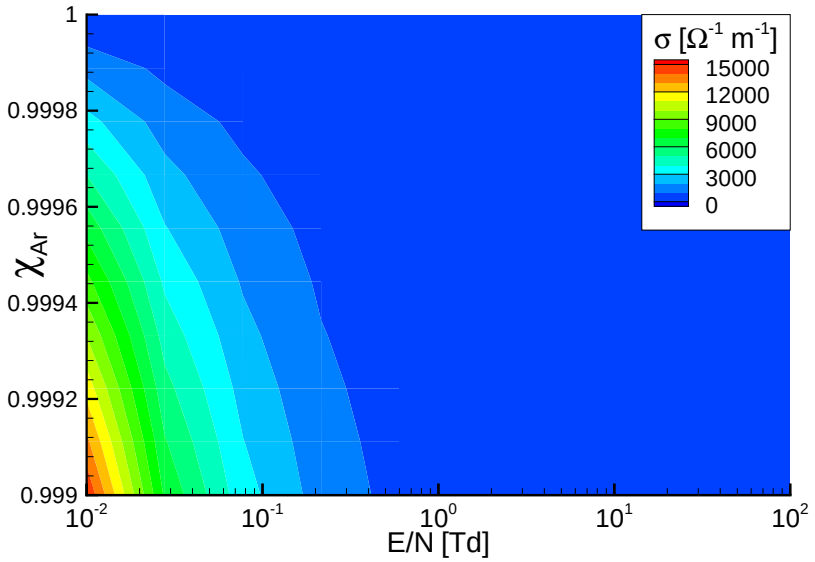

Figure 8. Electrical conductivity contours for weakly-ionized argon.

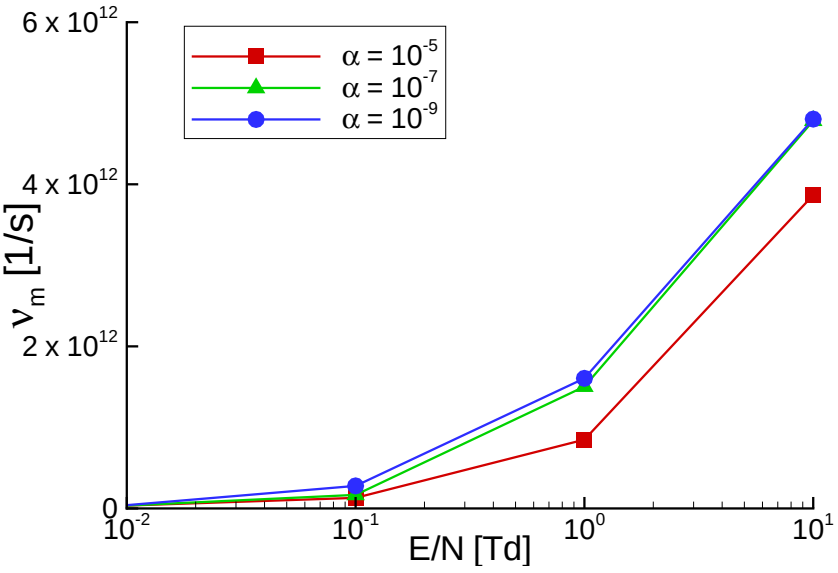

Figure 9. Electron collision frequency for weakly-ionized argon at $p = 1$ atm.

$$\ln\left(\frac{\alpha}{\sigma}\right) = f\left(\mathrm{E}/N, \chi_{\mathrm{Ar}}, \chi_{\mathrm{Ar}^+}\right) \tag{14}$$

Applying the natural logarithm function provides a second advantage when the model is employed. Since the formulated model is a function of the natural logarithm and the degree of ionization, the electrical conductivity must be extracted from the model solution by dividing the degree of ionization by the exponential function of the model's prediction: $\sigma = \alpha / \exp\left(\mathbf{PRS}\left(\mathrm{E}/N, \chi_{\mathrm{Ar}}, \chi_{\mathrm{Ar}^+}\right)\right)$. Since the exponential of any real number (the result of using the PRS model), is positive, the resulting electrical conductivity predicted will always be greater than or equal to zero. This characteristic (the model will always provide a positive value), is critical for the implementation of the model in the MHD module, since the electrical conductivity of a real gas is always greater than or equal to zero.

Although this formulation of the model incurs additional computational expense (i.e., evaluation of the exponential function), higher accuracy is achieved for lower order PRS models because the DOE's surface gradients are reduced. The model accuracy is determined by computing the Mean Absolute Error (MAE) and the Mean Absolute Percent Error (MAPE):

$$\text{Mean Absolute Error (MAE)} = \frac{1}{n}\sum_{i=1}^{n}\left|\hat{\sigma} - \sigma\right|_i \tag{15}$$

$$\text{Mean Absolute Percent Error (MAPE)} = \frac{1}{n}\sum_{i=1}^{n}\left|\frac{\hat{\sigma} - \sigma}{(\hat{\sigma} + \sigma)/2}\right|_i \tag{16}$$

where $\hat{\sigma}$ is the solution computed by the Boltzmann solver and σ is the solution computed by the model. The percent error is the normalized percent error to remove the bias when evaluating an over-prediction.[62] A summary of the surrogate response surface model performance metrics is tabulated in Table 1.

Table 1. Summary of surrogate model performance metrics.

Surrogate	MAPE	MAE	coefficients	conservativeness
PRS - 2$^{\text{nd}}$ order	16.35 %	90.72 $\Omega^{-1}\mathrm{m}^{-1}$	10	100%

The 2nd order PRS model with its coefficients is listed in equation (17).

$$\begin{aligned}\sigma = &- 842.64 + 128.02(\mathrm{E}/N) + 2558.28(\chi_{\mathrm{Ar}}) - 4112.52(\chi_{\mathrm{Ar}^+}) \\ &- 4.82(\mathrm{E}/N)^2 - 118.25(\mathrm{E}/N)(\chi_{\mathrm{Ar}}) - 121.33(\mathrm{E}/N)(\chi_{\mathrm{Ar}^+}) \\ &- 1732.34(\chi_{\mathrm{Ar}})^2 + 3229.51(\chi_{\mathrm{Ar}})(\chi_{\mathrm{Ar}^+}) - 7342.51(\chi_{\mathrm{Ar}^+})^2\end{aligned} \tag{17}$$

where E/N is normalized from 0 to 1 for a range of 0.01 to 100 Td. (1 Td = 10^{-17} V·cm^2)

E. Viscosity Model

Chemically non-reacting, thermodynamic equilibrium simulations are computed using the variable hard sphere (VHS) viscosity model. The VHS model is used because the viscosity is assumed to only be a function of temperature, since the species present (argon, argon ion, and electrons), have a single energy mode and are chemically non-reacting:

$$\mu = \mu_{ref}\left(\frac{T}{T_{ref}}\right)^{\omega} \tag{18}$$

where μ is the viscosity, the reference viscosity coefficient, $\mu_{ref} = 2.117 \times 10^{-5}$ N s/m^2, for a reference temperature, $\mathrm{T}_{ref} = 273$ K, and a viscosity index, $\omega = 0.81$. This method, as outlined by Schwartzentruber *et al.*,[63] requires several reference coefficients which are listed in Ref. 56.

III. Results

Three-dimensional calculations are carried out for Mach 4.75 argon flow over a hemisphere-shaped forebody attached to a cylinder, which was originally studied experimentally by Kranc *et al.*[10] The forebody hemisphere has a radius of 1.5 inch ($r_n = 0.0381$ m), and the geometry is mounted parallel to the freestream, as seen in Fig. 10. The freestream flow is composed of strongly ionized argon (the degree of ionizion was estimated by Kranc *et al.* as $\alpha = 0.025$), which is produced by a plasma torch (direct-current arc-heater). The heater is located before the converging-diverging nozzle, which accelerates the gas into the test chamber. Kranc *et al.* state that the electrons are 'frozen' in the nozzle, and that the flow is not chemically reacting after it is initially ionized by the heater. The flow conditions reported by Kranc *et al.* are listed in Table 2.

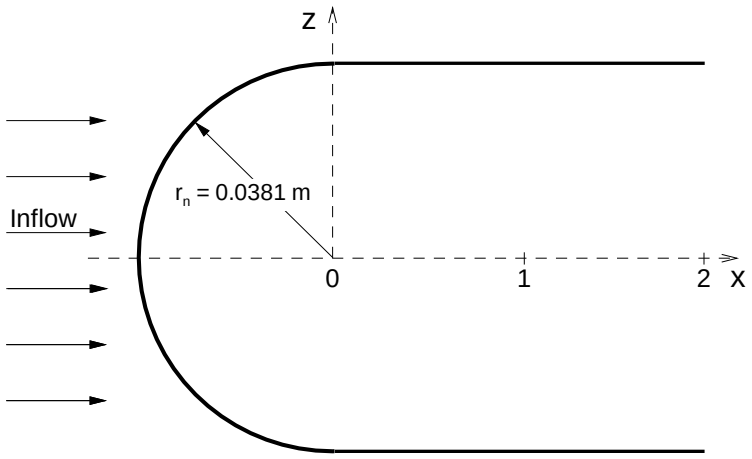

Figure 10. Hemisphere capped geometry. Adapted from.[10]

Table 2. Flow conditions for the MHD-Heat Shield experiment as reported by Kranc *et al.*[10]

Parameter	Value	
M	4.75	
u_∞	3000.0	$^{m}/_{s}$
T_∞	1100.0	K
T_w	300.0	K
p_∞	27.8	Pa
ρ_∞	1.035×10^{-4}	$^{kg}/_{m^3}$
n_e	4×10^{19}	m^{-3}
α	0.025	
r_n	0.0381	m
μ_∞	8×10^{-5}	$^{kg}/_{m \cdot s}$
Re_L	3880	m^{-1}
Re	148	

A structured grid is generated, but is decomposed into two grid domains because of the hemispherical forebody. The first domain includes the forebody, while the second accommodates the rest of the geometry. While the baseline flow solution (the flow without the magnetic field), is axisymmetric, the rest of the simulations are computed using a three-dimensional grid because the MHD routine developed is currently only implemented for three-dimensional domains.

The grid is generated with equal spacing along the hemisphere portion of the geometry (first domain),

and gradually increases in spacing along the remaining surface (second domain). Grid points are equally spaced around the circumference of the geometry and the radial points are algebraically spaced to increase the number of points close to the body. As a result, cell clustering occurs primarily in the hemispherical forebody and near the body surface. The baseline grid uses 50 points along the body (30 in the hemispherical region), 30 points along one quarter of the circumference, and 30 radial points. Two refined grids are also developed and used in the grid-independence study, giving the following set of computational meshes: $50 \times 30 \times 30$ (coarse), to $100 \times 60 \times 60$ (medium), to $200 \times 120 \times 120$ (fine).

Figure 11 plots the pressure coefficient and nondimensional heat flux for the baseline flow along the surface of the geometry, as defined in equations (19) and (20), respectively:

$$\mathrm{C_p} = \frac{p_w - p_\infty}{1/2\rho_\infty u_\infty^2} \tag{19}$$

$$\mathrm{C_h} = \frac{q_w}{1/2\rho_\infty u_\infty^3} \tag{20}$$

where (q_w) is the total heat flux to the wall. The grid-independence study shows little difference between the 'medium' and 'fine' grids, therefore the 'medium' grid is considered sufficiently refined and is used in the rest of the analysis. However, the MHD module might require its own grid resolution study.

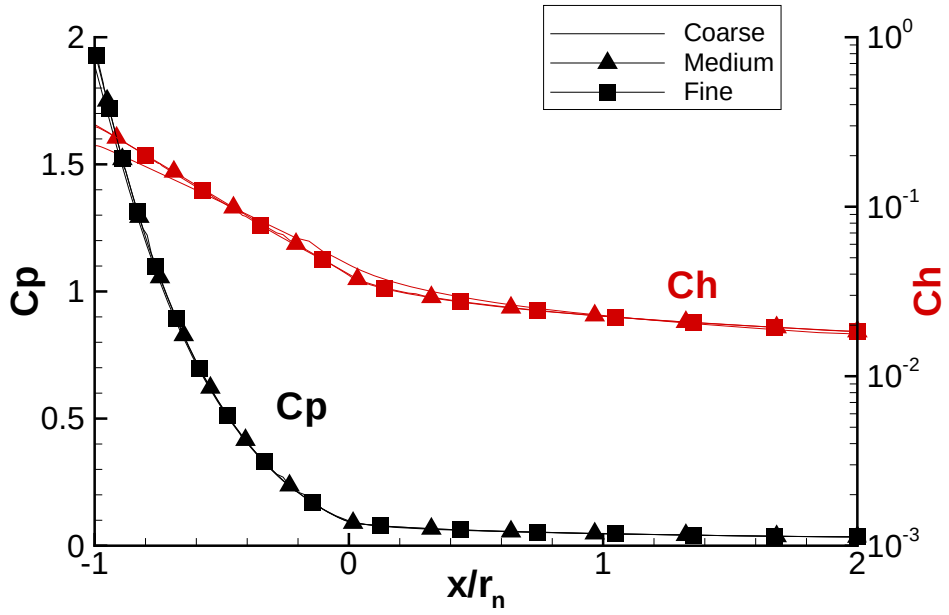

Figure 11. Nondimensional pressure and heat flux along the surface of Mach 4.75 argon flow around a hemisphere capped geometry for various grids.

A closer examination of the freestream conditions, specifically, the degree of ionization, reveals α was estimated by Kranc *et al.* using tables from Arave and Huseley,[64] along with the stagnation temperature and pressure. While this approach may be approximately correct, the degree of ionization is better estimated by using the Saha equation for a singly ionized atomic gas:[65]

$$\frac{\alpha^2}{1-\alpha^2}\, p = 3.16 \times 10^{-7}\ \mathrm{T}^{5/2}\ \exp\left(-\frac{\varepsilon_i}{k\mathrm{T}}\right) \tag{21}$$

where p is the pressure in atmospheres, T is the temperature in Kelvin, Boltzmann's constant is 1.3807×10^{-23} J/K, and ε_i is the ionization energy required to remove the electron from the atom in the gas considered. The ionization potential for argon, $\varepsilon_i = 2.53 \times 10^{-18}$ J, and the stagnation pressure and temperature are 0.49 atm and 9700 K, respectively. Using the Saha equation yields a degree of ionization $\alpha = 0.00623$.

This new estimate for the degree of ionization only changes two values listed in Table 2, namely, $\alpha = 6.23 \times 10^{-3}$ and $n_\mathrm{e} = 1 \times 10^{19}$ m^{-3}, which results in a slight modification to the freestream conditions, as seen in Table 3.

Table 3. Modifications to the freestream conditions for the MHD-Heat Shield experiment of Kranc *et al.*[10]

	Value	
Parameter	**Reported**	**Adjusted**
u_∞ [m/s]	3000	3000
T_∞ [K]	1100	1100
T_w [K]	300	300
α	0.025	0.00623
ρ_{Ar} [kg/m^3]	1.01×10^{-4}	1.09×10^{-4}
ρ_{Ar^+} [kg/m^3]	2.65×10^{-6}	6.85×10^{-7}
ρ_e [kg/m^3]	3.64×10^{-11}	9.41×10^{-12}

Since the changes to the individual species densities are minimal, and the flow is assumed chemically non-reacting, these slight adjustments to the freestream conditions are assumed not to noticeably alter the resulting flow-field. Therefore, the 'medium' grid discussed previously is assumed to provide sufficient grid-independence and is used in the rest of the analysis. The remaining simulations reported in this section use the freestream conditions corresponding to $\alpha = 0.00623$.

Figure 12 plots the temperature contours for the flow without the magnetic field. As seen in the figure, the peak temperature is 9000 K, which is 150 K hotter than the solution computed using the freestream conditions corresponding to $\alpha = 0.025$. The temperature increase is the result of the slight increase in total density. Using the baseline flow-field solutions from both simulations (i.e. $\alpha = 0.025$ and 0.00623), the expected range of electrical conductivity, estimated from the models presented in the previous section, is displayed in Table 4. The results indicate slight discrepancies in estimated electrical conductivities, with the 2nd order PRS predictions residing between the semi-empirical models.

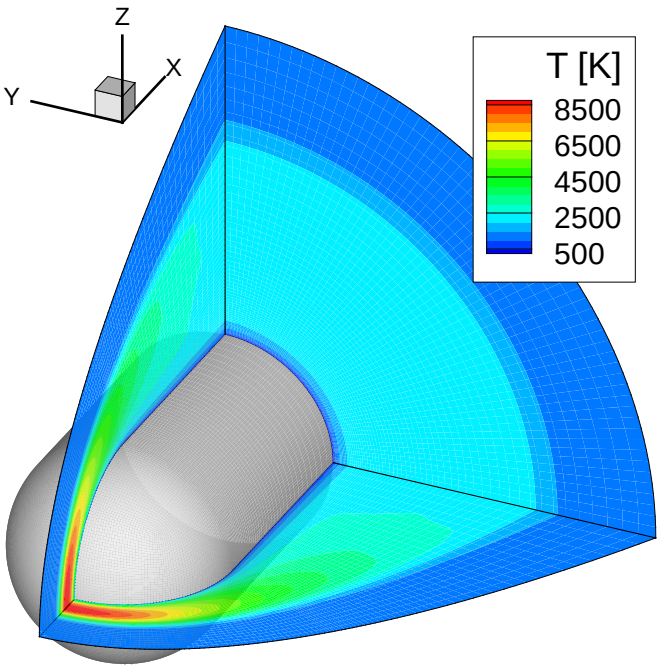

Figure 12. Temperature contours for Mach 4.75 argon flow around a hemisphere capped geometry. ($\alpha = 0.00623$)

In the experiment of Kranc *et al.*, the applied magnetic field is produced by an electromagnet located inside the hemisphere-shaped forebody, that can be approximated by a dipole. The magnetic field decays as r^{-3} from its centroid, which is assumed to be located along the x-axis, where the forebody merges with the

Table 4. Electrical conductivity estimates for the MHD-Heat Shield experiment without an applied magnetic field. (E/$N = 0$)

σ $[\Omega^{-1}\mathbf{cm}^{-1}]$	$\alpha = 0.025$	$\alpha = 0.00623$
Raizer	0 - 1.4	0 - 1.5
Chapman and Cowling	17.7 - 50.4	4.4 - 24.2
2^{nd} order PRS	0.1 - 0.2	7.1 - 8.1

rest of geometry ($\mathrm{x/r_n} = 0$), as seen in Fig. 13. The magnetic field contours are nondimensionalized by the peak magnetic field strength, $\mathrm{B_{max}}$, which occurs at the stagnation point ($\mathrm{x/r_n} = -1$ for the configuration shown in Fig. 13). Note that the peak magnetic field strength is used to designate each simulation for the rest of this analysis.

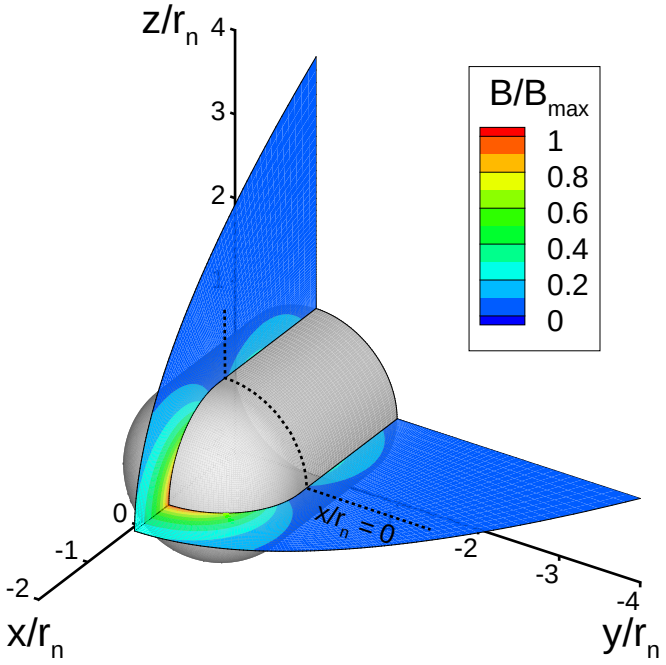

Figure 13. Nondimensional dipole magnetic field contours from a magnet located in the hemisphere capped geometry.

In Cartesian coordinates, the dipole magnetic field is:

$$\mathbf{B} = \mathrm{B_{max}} \frac{\cos\theta}{2} \frac{\mathrm{r_n^3}}{\mathrm{r^5}} \begin{bmatrix} \mathrm{r}^2 - x^2 \\ -3xy \\ -3xz \end{bmatrix}$$

where the angle $\theta = \arcsin(\sqrt{y^2 + z^2}/\mathrm{r})$.

The flow-field around the geometry (without the applied magnetic field), is axisymmetric and steady, as evident in the temperature contours seen in Fig. 12. This means the electric current must only travel in the azimuthal direction (perpendicular to the incoming flow, around the axis of symmetry), and the electric field must be zero.[4] This reduces the magnetic force in the momentum equation to $\tilde{\sigma} \cdot (\mathbf{u} \times \mathbf{B}) \times \mathbf{B}$, and sets the energy deposition term in the total energy equation to zero, $\mathbf{j} \cdot \mathbf{E} = 0$. Note that Joule heating is still present under these assumptions, $\gamma(\mathbf{E} + \mathbf{u} \times \mathbf{B}) \cdot \mathbf{j} \neq 0$. Since the electric field is assumed zero and the magnetic field is applied, only the current density field ($\mathbf{j} = \tilde{\sigma} \cdot [\mathbf{u} \times \mathbf{B}]$), needs to be updated in the MHD module.

Simulations are carried out for several magnetic field strengths and electrical conductivity models. The simulations start from the steady-state 'baseline' solution (without an applied magnetic field), and iterate

until the flow-field has achieved a new steady-state (converged). Steady-state is assumed once the L2 residual error from the conservation equations decays to the minimum allowed by machine precision zero, as seen in Fig. 14 for a typical simulation. In this scenario, at least 10 characteristic flow times worth of time steps are required to achieve a steady-state flow-field solution. A characteristic flow time is defined as the time it takes for the flow to traverse the length of the geometry (i.e. flow time = L/u_∞).

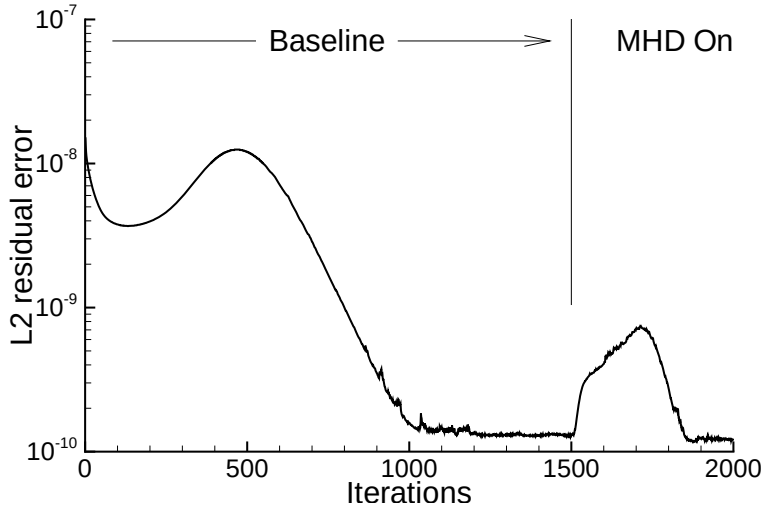

Figure 14. L2 residual error from a simulation of Mach 4.75 argon flow around a hemisphere capped geometry with a 0.13 T magnet. (Chapman and Cowling conductivity model)

The assumption that the electric field is negligible ($\mathbf{E} = 0$), is verified by simulating the flow with and without computing the electric field. The Chapman and Cowling electrical conductivity model is employed for both simulations with $B_{max} = 0.28$ T. The MHD module is used to update the electric field every 5 fluid iterations. Figure 15 plots the temperature contours and current lines for both scenarios. As seen in the figures, computing $\mathbf{E}$ from the MHD module does not alter the flow structure or current lines.

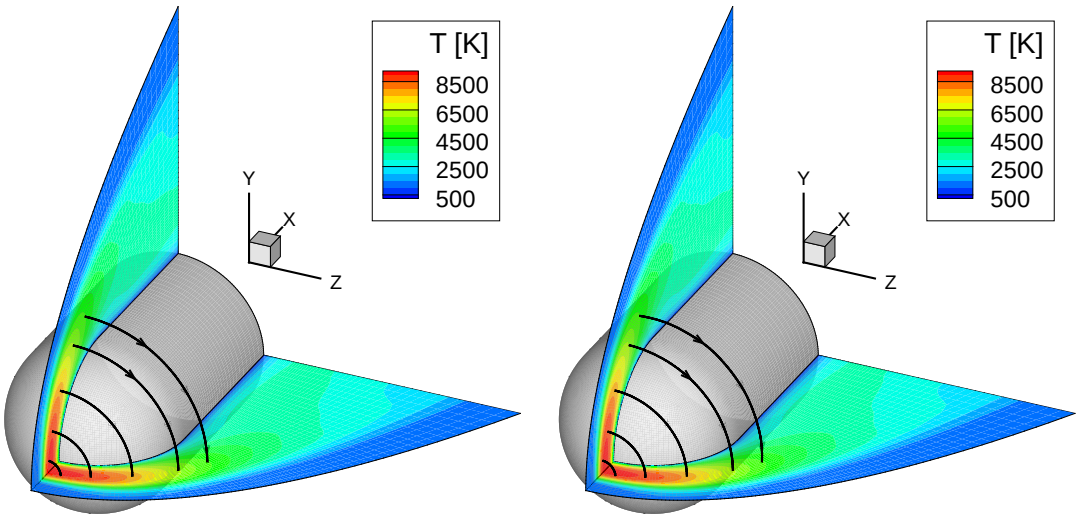

(a) Assuming $\mathbf{E} = 0$. (b) Computing $\mathbf{E}$.

Figure 15. Temperature contours and current lines for Mach 4.75 argon flow around a hemisphere capped geometry with a 0.28 T magnetic field. Chapman and Cowling conductivity model)

Kranc *et al.* reported an increase in shock standoff distance due to the applied magnetic field.[10] The increase was measured by comparing photographs of the flow with and without the applied magnetic field. In their analysis, they assume the upstream edge of the shock can be inferred from the boundary of the flow's

luminosity. This photographic technique for measuring the shock standoff distance was previously used by Ziemer[8] and Bailey and Sims[66] in similar experiments.

Although the computational solutions provide many ways of estimating the shock location, the change in shock standoff distance is computed by comparing the location, along the stagnation line, where the density ratio exceeds the ideal gas, infinite Mach number threshold for a normal shock wave:

$$\lim_{M_1 \to \infty} \frac{\rho_2}{\rho_1} = \lim_{M_1 \to \infty} \frac{(\gamma+1)M_1^2}{(\gamma-1)M_1^2+2} = \frac{\gamma+1}{\gamma-1} \tag{22}$$

where M_1 is the upstream Mach number, γ is the ratio of specific heats, ρ_1 is the upstream density, and ρ_2 is the downstream density. Using this equation, the density ratio limit for argon is 4 ($\gamma = 5/3$). This approach provides a consistent method for defining the shock location, so it should provide adequate estimates of the change in shock standoff distance due to an applied magnetic field. Figure 16 plots the density ratio contours for the electrical conductivity models with a peak magnetic field of 0.13 T (1 telsa = 10^4 gauss [G]).

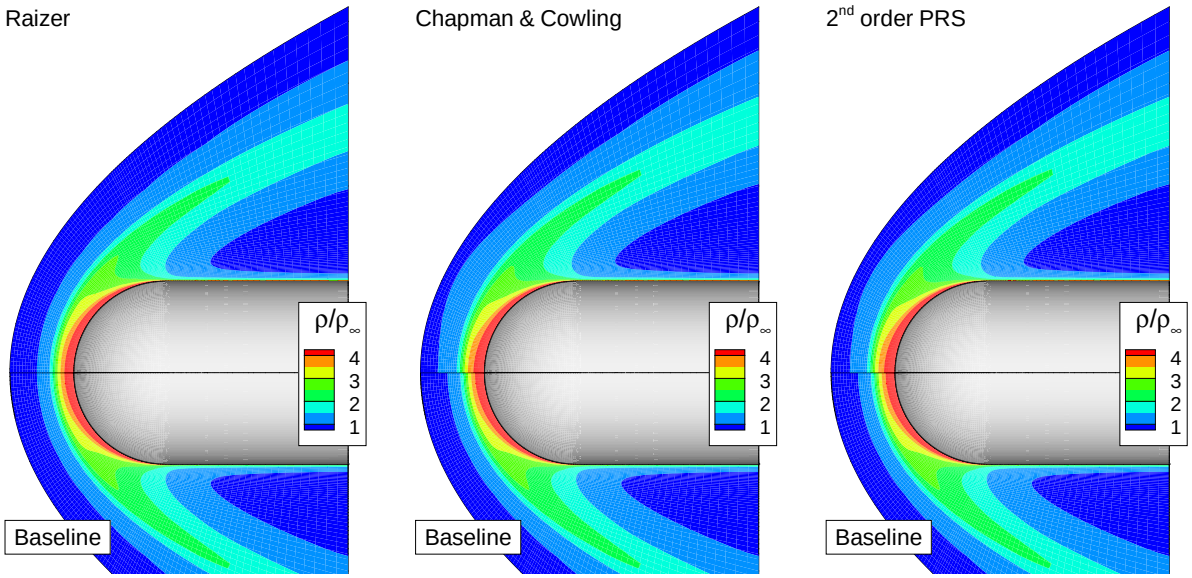

(a) Raizer (b) Chapman and Cowling (c) 2nd order PRS

Figure 16. Density ratio contours for Mach 4.75 argon flow around a hemisphere capped geometry for various electrical conductivity models. ($B_{max} = 0.13$ T)

The change in shock standoff distance is computed for the various models, and plotted in Fig. 17 with experimental measurements collected using the photographic technique described previously.

The experimental uncertainty was ±10% (error in determining shock location for one run), but the repeatability (difference in shock location between nominally identical runs) was ±30% as seen for $B_{max}^2 \simeq 13 \times 10^6$ G^2. Both the 2nd order PRS model and Chapman and Cowling models match the experimental data well, with the 2nd order PRS model fitting much better, particularly at larger magnetic field strengths. Solutions obtained by using Raizer's model observed almost no change in shock standoff distance because the model predicts a lower range of electrical condicitivities (as seen in Table 4). In addition, Raizer's model is only temperature dependant, so its peak conductivity is just downstream of the bow shock (where the temperature is the highest), yet the magnetic field strength has already significantly decayed due to its r^{-3} dependency.

The heat transfer to the surface for the various electrical conductivity models is shown in Fig. 18. Integrating the heat flux over the surface produces the total heating to the geometry. The change in peak heating is computing by comparing the heat flux at the stagnation point ($\Delta q_w = \frac{q_{w,MHD} - q_{w,baseline}}{q_{w,baseline}}$). Table 5 lists the percent change in peak heat flux and total heating for various magnetic field strengths and electrical conductivity models.

Except for the results from Raizer's model, the total heating to the surface actually slightly increases because of increased heating to the cylindrical portion of the geometry (i.e. aft of the stagnation region),

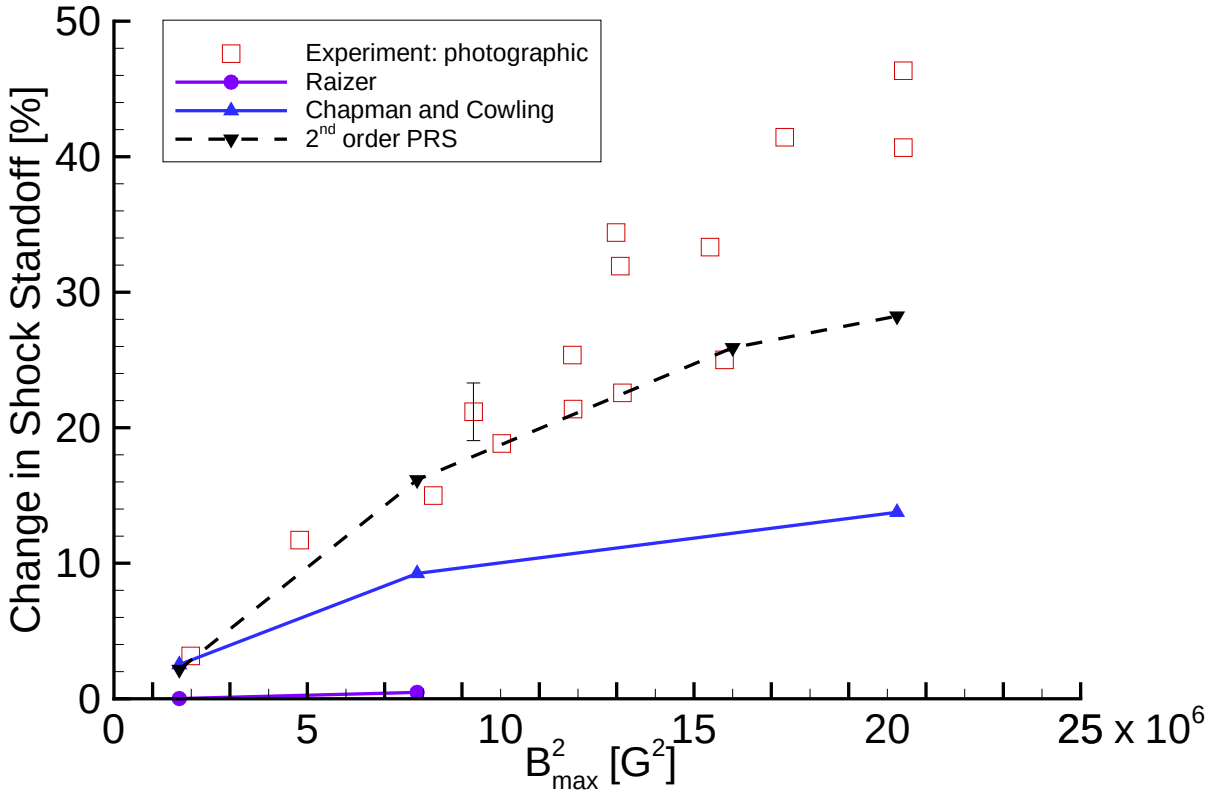

Figure 17. Percent change in shock standoff distance versus magnetic field strength for Mach 4.75 argon flow around a hemisphere capped geometry with various electrical conductivity models. Measurements from.[10] (experimental uncertainty ±10%)

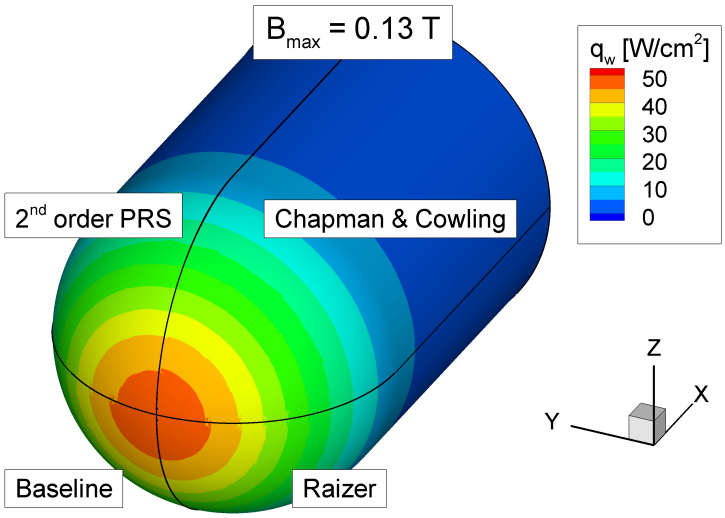

Figure 18. Heat flux contours for Mach 4.75 argon flow around a hemisphere capped geometry with a 0.13 T magnetic field and various electrical conductivity models.

Table 5. Percent change in heat flux to the surface for Mach 4.75 argon flow around a hemisphere capped geometry with an MHD-Heat Shield.

	Δ Total Heating		Δ Peak Heating	
Model	B = 0.13 T	B = 0.28 T	B = 0.13 T	B = 0.28 T
Raizer	-0.1 %	-0.3 %	-0.3 %	-1.2 %
Chapman and Cowling	0.6 %	1.5 %	-1.6 %	-6.3 %
2^{nd} order PRS	0.4 %	1.1 %	-2.5 %	-5.6 %

due to the direction of the magnetic field lines in the region where the hemisphere capped forebody merges with the cylindrical aft section. Raizer's model fails to capture this behavior because its predicted electrical conductivity is too low throughout the domain, but particularly in the aft region where the freestream temperature is much cooler than in the bow shock. In general, an applied magnetic field moderately increases the total heating to the geometry, but significantly decreases the peak heat flux at the stagnation point. Both the 2^{nd} order PRS model and the Chapman and Cowling model yield similar results, but since the 2^{nd} order PRS model provides better estimates in the percent change in shock standoff distance, its results for the heat flux to the geometry may be more accurate.

IV. Conclusions

Newly developed computational tools were used to compute hypersonic flow around a hemisphere capped geometry which utilizes a magnet located within the body as a means of heat flux mitigation. These tools include an improved electrical conductivity model and a parallelized 3D MHD module that is loosely coupled to a 3D fluid code. In addition, the Hall effect was implemented and verified by investigating flow between finite electrodes.

A Mach 4.75 argon flow over a hemisphere-shaped forebody attached to a cylinder was then explored, corresponding to the experiment of Kranc *et al.*. The magnetic field worked to oppose and slow the flow near the stagnation region, and increased the shock standoff distance. The increase in shock standoff distance decreased the peak heating to the body (at the stagnation point), but also increased the total heating to the geometry because of increased heating to the cylindrical portion of the body. This result has important implications for design of MHD-Heat Shield devices: they can reduce peak heat loads, but with a potential penalty in total heating. Since both peak and total heat load are important aspects to consider when designing a thermal protection system, this technology provides additional scenarios for vehicle designers to evaluate.

Acknowledgments

The authors are indebted to the Michigan/AFRL/Boeing Collaborative Center in Aeronautical Sciences which provides funding to the first author. The first author would like to thank Professor Mark Kushner for his valuable discussions on electrical conductivity and the use of his Boltzmann solver.

References

[1]Kantrowitz, A. R., "A Survey of Physical Phenomena Occurring in Flight at Extreme Speeds," *Proceedings of the Conference on High-Speed Aeronautics*, edited by A. Ferri, N. J. Hoff, and P. A. Libby (Polytechnic Institute of Brooklyn, New York, 1955), pp. 335 – 339.

[2]Resler, E. L. and Sears, W. R., "The Prospects for Magneto-Aerodynamics," *Journal of Aeronatuical Sciences*, Vol. 25, April 1958, pp. 235–245, 258.

[3]Resler, E. L. and Sears, W. R., "The Prospects for Magneto-Aerodynamics Correction and Addition," *Journal of Aero/Space Sciences*, Vol. 26, No. 5, May 1959, pp. 319.

[4]Bush, W. B., "Magnetohydrodynamic-Hypersonic Flow Past a Blunt Body," *Journal of Aerospace Sciences*, Vol. 25, 1958, pp. 685.

[5]Bush, W. B., "The Stagnation-Point Boundary Layer in the Presence of an Applied Magnetic Field," *Journal of Aerospace Sciences*, Vol. 28, No. 8, August 1961, pp. 610–611, 630.

[6]Poggie, J. and Gaitonde, D. V., "Magnetic Control of Flow Past a Blunt Body: Numerical Validation and Exploration," *Physics of Fluids*, Vol. 14, No. 5, May 2002, pp. 1720–1731.

[7]Coakley, J. F. and Porter, R. W., "Time-Dependent Numerical Analysis of MHD Blunt Body Problem," *AIAA Journal*, Vol. 9, No. 8, August 1971, pp. 1624–1626.

[8]Ziemer, R. W., "Experimental Investigations in Magnetoaerodynamics," *Journal of American Rocket Society*, Vol. 29, No. 9, 1959, pp. 642.

[9]Wilkinson, B., "Magnetohydrodynamic Effects on Stagnation-Point Heat Transfer from Partially Ionized Nonequilibrium Gases in Supersonic Flow," *Engineering Aspects of Magnetohydrodynamics: Proceedings, 3rd Symposium*, edited by N. W. Mather and G. W. Sutton (Gordon and Breach, New York, 1964), pp. 413 − 438.

[10]Kranc, S., Yuen, M. C., and Cambel, A. B., "Experimental Investigation of Magnetoaerodynamic Flow around Blunt Bodies," Tech. rep., National Aeronautics and Space Administration, Washington, D.C., August 1969, NASA CR-1392.

[11]Nowak, R. J., Kran, S., Porter, R. W., Yuen, M. C., and Cambel, A. B., "Magnetogasdynamic Re-Entry Phenomena," *Journal of Spacecraft*, Vol. 4, No. 11, November 1967, pp. 1538–1542.

[12]Nowak, R. J. and Yuen, M. C., "Heat Transfer to a Hemispherical Body in Supersonic Argon Plasma," *AIAA Journal*, Vol. 11, No. 11, November 1973, pp. 1463–1464.

[13]Porter, R. W. and Cambel, A. B., "Hall Effect if Flight Magnetogasdynamics," *AIAA Journal*, Vol. 5, No. 12, December 1967, pp. 2208–2213.

[14]Romig, M. F., "The Influence of Electric and Magnetic Fields on Heat Transfer to Electrically Conducting Fluids," *Advances in Heat Transfer*, edited by T. F. Irvine and J. P. Hartnett (Academic, New York, 1964), Vol. 1, pp. 267 − 354.

[15]Padilla, J. F., *Assessement of Gas-Surface Interaction Models for Computation of Rarefied Hypersonic Flows*, 2008, PhD thesis, Department of Aerospace Engineering, University of Michigan.

[16]Fomin, V. M., Tretyakov, P. K., and Taran, J.-P., "Flow Control using Various Plasma and Aerodynamic Approaches," *Aerospace Science and Technology*, Vol. 8, No. 5, July 2004, pp. 411–421.

[17]Shang, J. S., Surzhikov, S. T., Kimmel, R., Gaitonde, D., Menart, J., and Hayes, J., "Mechanisms of Plasma Actuators for Hypersonic Flow Control," *Progress in Aerospace Sciences*, Vol. 41, No. 8, November 2005, pp. 642–668.

[18]Bityurin, V., Bocharov, A., and Lineberry, J., "MHD Flow Control in Hypersonic Flight," *13th International Space Planes and Hypersonic Systems Technologies Conference*, AIAA Paper 2005-3225, 2005.

[19]Palmer, G., "Magnetic Field Effects on the Computed Flow over a Mars Return Aerobrake," *Journal of Thermophysics and Heat Transfer*, Vol. 7, No. 2, April-June 1993, pp. 294–301.

[20]Bisek, N. J., Boyd, I. D., and Poggie, J., "Numerical Study of Plasma-Assisted Aerodynamic Control for Hypersonic Vehicles," *Journal of Spacecraft and Rockets*, Vol. 46, No. 3, May-June 2009.

[21]Kremeyer, K., Sebastian, K., and Shu, C.-W., "Computational Study of Shock Mitigation and Drag Reduction by Pulsed Energy Lines," *AIAA Journal*, Vol. 44, No. 8, August 2006, pp. 1720–1731.

[22]Yan, H. and Gaitonde, D., "Control of Edney IV Interaction by Energy Pulse," *44th AIAA Aerospace Sciences Meeting and Exhibit*, AIAA Paper 2006-562, 2006.

[23]Menart, J., Stanfield, S., Shang, J., Kimmel, R., and Hayes, J., "Study of Plasma Electrode Arrangements for Optimum Lift in a Mach 5 Flow," *44th AIAA Aerospace Sciences Meeting and Exhibit*, 2006, AIAA Paper 2006-1172.

[24]Girgis, I. G., Shneider, M. N., Macheret, S. O., Brown, G. L., and Miles, R. B., "Creation of Steering Moments in Supersonic Flow by Off-Axis Plasma Heat Addition," *40th AIAA Aerospace Sciences Meeting and Exhibit*, 2002, AIAA Paper 2002-129.

[25]Gnemmi, P., Charon, R., Dupéroux, J.-P., and George, A., "Feasibility Study for Steering a Supersonic Projectile by a Plasma Actuator," *AIAA Journal*, Vol. 46, No. 6, June 2008, pp. 1308–1317.

[26]Bityurin, V. A., Vatazhin, A. B., and Gus'kov, O. V., "Hypersonic Flow Past the Spherical Nose of a Body in the Presence of a Magnetic Field," *Fluid Dynamics*, Vol. 39, No. 4, July 2004, pp. 657–666.

[27]Miles, R. B., Macheret, S. O., Shneider, M. N., Steeves, C., Murray, R. C., Smith, T., and Zaidi, S. H., "Plasma-Enhanced Hypersonic Performance Enabled by MHD Power Extraction," *43th AIAA Aerospace Sciences Meeting and Exhibit*, AIAA Paper 2005-561, 2005.

[28]Katsurayama, H., Kawamura, M., Matsuda, A., and T., A., "Kinetic and Continuum Simulations of Electromagnetic Control of a Simulated Reentry Flow," *Journal of Spacecraft and Rockets*, Vol. 45, No. 2, March-April 2008, pp. 248–254.

[29]Hodara, H., "The Use of Magnetic Fields in the Elimination of the Re-Entry Radio Blackout," *Proceedings of the IRE*, Vol. 4, No. 12, December 1961, pp. 1825–1830.

[30]Kim, M., Keidar, M., and Boyd, I. D., "Analysis of an Electromagnetic Mitigation Scheme for Reentry Telemetry Through Plasma," *Journal of Spacecraft and Rockets*, Vol. 45, No. 6, November-December 2008, pp. 1223–1229.

[31]Macheret, S. O., Shneider, M. N., and Candler, G. V., "Modeling of MHD Power Generation on Board Reentry Vehicles," *42nd AIAA Aerospace Sciences Meeting*, AIAA Paper 2004-1024, 2004.

[32]Wan, T., Suzuki, R., Candler, G., Macheret, S., and Schneider, M., "Three Dimensional Simulation of Electric Field and MHD Power Generation During Re-Entry," *36th AIAA Plasmadynamics and Lasers Conference*, AIAA Paper 2005-5045, 2005.

[33]Fujino, T., Yoshino, T., and Ishikawa, M., "Prediction of Generator Performance and Aerodynamic Heating of Reentry Vehicle Equipped with On-board Surface Hall Type MHD Generator," *39th Plasmadynamics and Lasers Conference*, AIAA Paper 2008-4225, 2008.

[34]Linberry, J. T., Bityurin, V. A., and Vatazhin, A. B., "Cylinder with Current in Hypersonic Flow," *Proc. 3rd Workshop on Magneto-Plasma Aerodynamics in Aerospace Applications*, Institute of High Temperatures of RAS (IVTAN) (2001), pp. 15.

[35]Takizawa, Y., Sato, S., Abe, T., and Konigorski, D., "Electro-Magnetic Effect on Shock Layer Structure in Reentry-Related High-Enthalpy Flow," *35th AIAA Plasmadynamics and Lasers Conference*, AIAA Paper 2004-2162, 2004.

[36]Kimmel, R., Hayes, J., Menart, J., and Shang, J., "Supersonic Plasma Flow Control Experiments," Tech. rep., U.S. Air Force Research Laboratory, Wright-Patterson AFB, OH, December 2005, ARFL-VA-WP-TR-2006-3006.

[37]Matsuda, A., Kawamura, M., Takizawa, Y., Otsu, H., Konigorski, D., Sato, S., and Abe, T., "Experimental Investigation of the Hall Effect for the Interaction between the Weakly-Ionized Plasma Flow and Magnetic Body," *45th Aerospace Sciences Meeting*, AIAA Paper 2007-1437, 2007.

[38]Gülhan, A., Esser, B., Koch, U., Siebe, F., Riehmer, J., Giordano, D., and Konigorski, D., "Experimental Verification of Heat-Flux Mitigation by Electromagnetic Fields in Partially-Ionized-Argon Flows," *Journal of Spacecraft and Rockets*, Vol. 46, No. 2, March-April 2009, pp. 274–283.

[39]Gaitonde, D. V. and Poggie, J., "An Implicit Technique for 3-D Turbulent MGD with the Generalized Ohm's Law," *32th AIAA Plasmadynamics and Lasers Conference*, AIAA Paper 2001-2736, 2001.

[40]Gaitonde, D. V., "A High-Order Implicit Procedure for the 3-D Electric Field in Complex Magnetogasdynamic Simulations," *Computers and Fluids*, Vol. 33, No. 3, March 2004, pp. 345–374.

[41]Gaitonde, D. V. and Poggie, J., "An Implicit Technique for Three-Dimensional Turbulent Magnetoaerodynamics," *AIAA Journal*, Vol. 41, No. 11, November 2003, pp. 2179–2191.

[42]Damevin, H.-M. and Hoffmann, K. A., "Numerical Simulations of Magnetic Flow Control in Hypersonic Chemically Reacting Flows," *Journal of Thermophysics and Heat Transfer*, Vol. 16, No. 4, October-December 2002, pp. 498–507.

[43]Scalabrin, L. C. and Boyd, I. D., "Development of an Unstructured Navier-Stokes Solver For Hypersonic Nonequilibrium Aerothermodynamics," *38th AIAA Thermophysics Conference*, AIAA Paper 2005-5203, 2005.

[44]Scalabrin, L. C. and Boyd, I. D., "Numerical Simulation of Weakly Ionized Hypersonic Flow for Reentry Configurations," *9th AIAA/ASME Joint Thermophysics and Heat Transfer Conference*, AIAA Paper 2006-3773, 2006.

[45]MacCormack, R. W. and Candler, G. V., "The solution of the Navier-Stokes Equations Using Gauss-Seidel Line Relaxation." *Computers and Fluids*, Vol. 17, No. 1, January 1989, pp. 135–150.

[46]Holman, T. D. and Boyd, I. D., "Numerical Investigation of the Effects of Continuum Breakdown on Hypersonic Vehicle Surface Properties," *40th AIAA Thermophysics Conference*, AIAA Paper 2008-3928, 2008.

[47]Shercliff, J., *A Textbook of Magnetohydrodynamics*, Pergamon Press, 1965.

[48]Gaitonde, D. V. and Poggie, J., "Elements of a Numerical Procedure for 3-D MGD Flow Control Analysis," *40th AIAA Aerospace Sciences Metting and Exhibit*, AIAA Paper 2002-198, 2002.

[49]Bisek, N. J., Boyd, I. D., and Poggie, J., "Numerical Study of Electromagnetic Aerodynamic Control of Hypersonic Vehicles," *47th AIAA Aerospace Sciences Meeting and Exhibit*, AIAA Paper 2009-1000, 2009.

[50]Bisek, N. J., Boyd, I. D., and Poggie, J., "Three Dimensional Simulations of Hypersonic MHD Flow Control," *40th AIAA Plasmadynamics and Lasers Conference*, AIAA Paper 2009-3731, 2009.

[51]Oliver, D. A. and Mitchner, M., "Nonuniform Electrical Conduction in MHD Channel," *AIAA Journal*, Vol. 5, No. 8, August 1967, pp. 1424–1432.

[52]White, F. M., *Viscous Fluid Flow, 3rd ed.*, 2006, McGraw-Hill.

[53]Lin, S.-C., Resler, E. L., and Kantrowitz, A., "Electrical Conductivity of Highly Ionized Argon Produced by Shock Waves," *Journal of Applied Physics*, Vol. 26, No. 1, January 1955, pp. 95–109.

[54]Raizer, Y. P., *Gas Discharge Physics*, Springer-Verlag, 1991.

[55]Cambel, A. B., *Plasma Physics and Magnetofluid-Mechanics*, McGraw-Hill, 1963, p. 171.

[56]Bird, G. A., *Molecular Gas Dynamics and the Direct Simulation of Gas Flows*, 1994, Oxford Science Publications.

[57]Bird, G. A., "Monte-Carlo Simulation in an Engineering Context," *Rarefied Gas Dynamics*, edited by S. S. Fisher, Vol. 74 of *Progress of Astronautics and Aeronautics*, AIAA, New York, 1981, pp. 239–255.

[58]Weng, Y. and Kushner, M. J., "Method for Including Electron-Electron Collisions in Monte Carlo Simulations of Electron Swarms in Partially Ionized Gases," *Physical Review A*, Vol. 42, No. 10, November 1990, pp. 6192–6200.

[59]Rockwood, S. D., "Elastic and Inelastic Cross Sections for Electron-Hg Scattering from Hg Transport Data," *Physical Review A*, Vol. 8, No. 5, November 1973, pp. 2348–2358.

[60]Rockwood, S. D., "Effect of Electron-Electron and Electron-Ion Collisions in Hg, $CO_2/N_2/He$, and CO/N_2 discharges," *Journal of Applied Physics*, Vol. 45, No. 12, December 1974, pp. 5229–5234.

[61]Viana, F. A. C. and Goel, T., *SURROGATES Toolbox User's Guide*, 2008.

[62]Makridakis, S., "Accuracy Measures: Theoretical and Practical Concerns," *International Journal of Forecasting*, Vol. 9, No. 4, December 1993, pp. 527–529.

[63]Schwartzentruber, T. E., Scalabrin, L. C., and Boyd, I. D., "Hybrid Particle-Coontinuum Simulations of Non-Equilibrium Hypersonic Blunt Body Flow Fields," *9th AIAA/ASME Joint Thermophysics and Heat Transfer Conference*, AIAA Paper 2006-3602, 2006.

[64]Arave, R. J. and Huseley, O. A., "Aerothermodynamic Properties of High Temperature Argon," Tech. rep., Boeing, Seattle, WA, February 1962, D2-11238.

[65]Messerle, H. K., *Magnetohydrodynamic Electrical Power Generation*, 1995, John Wiley & Sons, Inc.

[66]Bailey, A. B. and Sims, W. H., "Shock Detachment Distance for Blunt Bodies in Argon at Low Reynolds Number," *AIAA Journal*, Vol. 1, No. 12, December 1963, pp. 2867–2868.